

# Effect of Energy Density on the Microstructure and Properties of the CrFeCoNiNb High Entropy Cladded Layer

**Pengfang Song**

Qingdao University of Technology

**Fulin Jiang** (✉ [sdujiangfulin@gmail.com](mailto:sdujiangfulin@gmail.com))

Qingdao Technological University

**Yuling Wang**

Qingdao University of Technology

**Fazhan Yang**

Qingdao University of Technology

**Zhaolin Zhong**

Qingdao University of Technology

---

## Research Article

**Keywords:** Energy density, High entropy alloys, Microstructure, Mechanical properties, Corrosion resistant

**Posted Date:** June 28th, 2021

**DOI:** <https://doi.org/10.21203/rs.3.rs-636926/v1>

**License:**  This work is licensed under a Creative Commons Attribution 4.0 International License.

[Read Full License](#)

---

**Version of Record:** A version of this preprint was published at The International Journal of Advanced Manufacturing Technology on October 20th, 2021. See the published version at <https://doi.org/10.1007/s00170-021-08042-x>.

# Effect of energy density on the microstructure and properties of the CrFeCoNiNb high entropy cladded layer

Pengfang Song<sup>1</sup>, Fulin Jiang\*<sup>1,2</sup>, Yuling Wang<sup>1</sup>, Fazhan Yang<sup>1</sup>, Zhaolin Zhong<sup>1</sup>

(1. Key Laboratory of Laser Green Intelligent Manufacturing Technology, Shandong province, Qingdao University of Technology, Qingdao 266520, China;

2. Key Laboratory of High-efficiency Clean Machinery Manufacturing Ministry of Education, Shandong province, Shandong University, Jinan 250061, China)

**Abstract :** A synergistic combination of mechanical properties and corrosion resistance property is desired for most ocean engineering structural applications. In this paper, we prepared high entropy alloy (HEA) cladded layer of composition CrFeCoNiNb (atomic%). We aim to attain a balance between the mechanical property and the corrosion resistance property through adjusting the energy density. The prepared CrFeCoNiNb cladded layer with the energy density of 116.7J/mm<sup>2</sup> exhibited excellent mechanical properties and high corrosion resistance. The improved mechanical properties are attributed to the fine grain strengthening, solid solution strengthening and dispersion strengthening. Whereas the excellent corrosion resistance is due to the fine grained BCC single phase structure and the compact passivation film. The variation of the mechanical properties and corrosion resistance with different energy densities are attribute to the phase composition. The diffraction peak area of the main phase of BCC decreases first and then increases with the increase of energy density, which is the main reason that the hardness of the cladded layer follows the similar trend. The outcome of our research suggests that the prepared CrFeCoNiNb cladded layer could be explored to realise surface strengthening of load-bearing parts in marine engineering equipment.

**Key words:** Energy density; High entropy alloys; Microstructure; Mechanical properties; Corrosion resistant

## 1. Introduction

Alloying is a common way of imbuing materials with desirable properties. Traditional alloys are prepared in a way of adding a minor element to the main element. The HEA is composed of four or more elements with approximately equal

---

Corresponding author.

E-mail addresses: sdujiangfulin@gmail.com (Fulin Jiang)

molar ratio, and its configuration entropy is required to be greater than  $1.5R$ [1]. The final structure of HEA is not dominated by any one element. Due to its high entropy effect, lattice distortion effect, cocktail effect and hysteretic diffusion effect, the HEA has many advantages that traditional alloy cannot reach. However, the synergistic improvement of strength, toughness and corrosion resistance of the HEA is difficult to achieve, and there is no satisfactory solution so far.

Most failure of the marine working equipment starts from the surface of the key parts[2]. The marine engineering equipment such as ship stern shaft works in the environment of high salt, high humidity and high load for a long time. And the surface failure is prone to occur due to heavy mechanical load and serious corrosion. As shown in Fig. 1, during the operation of the stern shaft, the propeller end receives the maximum torque under the action of uniform radial load. In addition, corrosion fatigue fracture is more likely to occur here when it is corroded by  $Cl^-$  in seawater, which will cause damage to the ship. Surface modification and strengthening of key parts have become an urgent need to improve the service life of equipment. With the breakthrough of “the combination of strength and toughness”[3] in the research of FeCoNiCrMn HEA, the nano eutectic HEA material system represented by CrFeCoNiNb(x) emerged at the right moment. CrFeCoNiNb series HEA is expected to have both excellent mechanical properties and corrosion resistance property, based on Hall-Petch effect, high entropy effect, hysteresis diffusion effect and nanoscale passivating effect. And the CrFeCoNiNb series HEA coatings are expected to be used in marine equipment, aerospace industry, semiconductor and many other industrial fields [4].

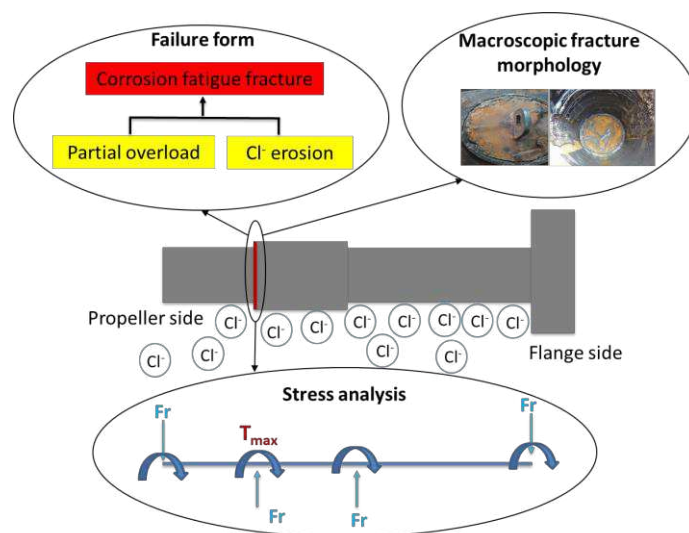


Fig.1. Failure analysis of stern shaft.

A few research has been conducted on the improvement of strength and toughness of FeCoNiCrNb coating. Maity et al. found that due to the addition of Nb element, the lamellar eutectic morphology fragments of CrCoNb generated would be embedded into the FeCoNiCr single-phase solid solution. The regular lamellar morphology was conducive to improving the structural stability and significantly improving the strength and toughness[5]. Another eutectic point of Co-Cr-Fe-Ni-M (M = Hf, Ta, Nb) system was successfully obtained by Xie et al., and the eutectic composition of the coating was thus changed. The eutectic HEA, previously composed of ductile FCC phase and brittle Laves phase, now has different area fractions and widths of FCC and Laves phases, resulting in improved mechanical properties[6]. Chaturvedi et al. explored the yield behavior after precipitation strengthening of the CrFeCoNiNb coating, and they found that the strong toughness was attributed to the strain hardening caused by  $\beta$  phase and the dislocation bypass mechanism caused by  $\gamma$  phase[7].

The excellent corrosion resistance of HEA coating depends on the stability of the passivation film and the number of galvanic cells on the other hand. In general, single-phase alloys are more resistant to corrosion than multiphase alloys. In addition, the coating with dense and uniform microstructure is more corrosion resistant than those with more impurities and component segregation. Most studies focus on the strength and toughness mechanism or the corrosion resistance of the existing CrFeCoNiNb coating. However, the synergistic combination of mechanical properties and corrosion resistance property is rarely reported. Tsau et al. reported that as a hard phase and corrosion resistance element, the addition of Nb can improve the hardness and corrosion resistance of the CrFeCoNiNb<sub>x</sub> coating[8]. Zhang et al. reported that with the increase of Nb content, the corrosion resistance and hardness of CoCrFeNb<sub>x</sub> coating are improved[9]. Wang et al. found that the corrosion resistance of the CoCrFeNi)<sub>95</sub>Nb<sub>5</sub> HEA coating was improved due to the formation of a dense passivating film consisting of Cr and Nb on the surface. At the same time, the mechanical properties are also significantly improved compared with the substrate[10].

Only a few research are carried out on the relationship between the preparation method[11] and the properties of the coating. Laser cladded technology[12] is a cost-effective additive preparation method, which has the characteristics of small heat affected zone, good directivity and good combination with substrate metallurgy, and it

is widely used in material processing. The performance of the coating will vary accordingly due to different heat absorption, even when the same kind of HEA coating is prepared with different laser energy density[13]. In this study, the synergistic improvement of the mechanical property and the corrosion resistance property of the CrFeCoNiNb HEA cladded layer is investigated through adjusting the energy density. The thermodynamic criterion of the applied CrFeCoNiNb is calculated to analyze whether CrFeCoNiNb cladded layer meets the criterion of forming a solid solution. The CrFeCoNiNb HEA cladded layers are prepared on the 42CrMo substrate with different energy densities. Then, the microstructure evolution, microhardness, wear morphology and corrosion behavior in 3.5wt.%NaCl solution of the prepared CrFeCoNiNb HEA cladded layers are observed. The influence of laser energy density on the mechanical properties and corrosion resistance of the HEA cladded layers were also explored.

## 2. Thermodynamic criterion

Laser cladded is a fast cooling and fast heating process with typical non - equilibrium solidification characteristics. The phase composition of the multi-component laser cladded layer in a typical non-equilibrium process could be predicted by the valence electron concentration ( $VEC$ ), electronegativity ( $\Delta\chi$ ), atomic size difference ( $\delta$ ), mixing enthalpy ( $\Delta H_{mix}$ ), configuration entropy ( $\Delta S_{conf}$ ) and laser energy ratio ( $K$ ). The  $\delta$  and  $\Delta\chi$  are a measure of the tendency to form intermediate compounds rather than primary solid solutions[14]. The  $\Delta H_{mix}$  shows a tendency to be ordered or cluster, and the  $\Delta S_{conf}$  shows a tendency[15] to form disordered solid solutions at a given temperature. Entropy and enthalpy are not independent, and they both strongly depend on the composition of the alloy. Although entropy and enthalpy act on the free energy together, Yeh[16] and his colleagues believe that with the increase of the number of elements in the alloy, the effect of entropy on the free energy will overcome the effect of enthalpy, thus stabilizing the solid solution. These expressions are as follows:

$$\delta = \sqrt{\sum_{i=1}^n c_i \left(1 - \frac{r_i}{\bar{r}}\right)^2} \quad (1-1)$$

$$\Delta\chi = \sqrt{\sum_{i=1}^n c_i (\chi_i - \bar{\chi})^2} \quad (1-2)$$

$$VEC = \sum_{i=1}^n c_i (VEC)_i \quad (1-3)$$

$$K = \frac{P}{D \cdot v} \quad (1-4)$$

$$\Delta S_{\text{conf}} = -R \sum_{i=1}^n c_i \ln c_i \approx R \ln n \quad (1-5)$$

$$\Delta H_{\text{mix}} = \sum_{i=1, i \neq j}^n \Omega_{ij} c_i c_j \quad (1-6)$$

$$\Delta G = \Delta H_{\text{mix}} - T \cdot \Delta S_{\text{conf}} \quad (1-7)$$

Where  $n$  represents the number of alloy components,  $c_i$  and  $c_j$  are the mole percentages of  $i$  and  $j$  components in the alloy,  $r_i$  is the  $i$ -th atomic radius,  $\bar{r} = \sum_{i=1}^n c_i r_i$  is the average atomic radius,  $\chi_i$  is the Pauling electronegativity of the  $i$ -th element,  $(VEC)_i$  represents the valence electron concentration of a single element,  $P$  is the laser power,  $D$  is the spot diameter,  $v$  is the scanning speed,  $R$  is the air constant  $8.314 \text{ J}/(\text{mol} \cdot \text{K})$ ,  $\Omega_{ij} = 4\Delta H_{AB}^{\text{mix}}$  is the interaction parameters of the two components,  $\Delta H_{AB}^{\text{mix}}$  is the binary mixing enthalpy,  $T$  is the absolute temperature, and  $\Delta G$  is the Gibbs free energy.

The data in Table 1 lists the binary mixing enthalpy. It can be seen that the mixing enthalpy between the elements does not have a positive value, that is, there is no repulsive reaction between the elements.

Table. 1 Values of  $\Delta H_{\text{mix}ij}$  ( $\text{Kj/mol}$ ) calculated using Miedema's model for atomic pairs

Element	Fe	Co	Cr	Ni	Nb
Fe	-	-1	-1	-2	-16
Co	-	-	-4	0	-25
Cr	-	-	-	-7	-7
Ni	-	-	-	-	-30
Nb	-	-	-	-	-

The data in Table 2 are calculated based on the above-mentioned Boltzmann system entropy assumption formula, which meets the standard proposed by Zhang et al[17]. according to the hume-rothery rule[18] :  $11 \leq \Delta S_{\text{mix}} \leq 19.5 \text{ J} \cdot \text{K}^{-1} \cdot \text{mol}^{-1}$  ,  $-22 \leq \Delta H_{\text{mix}} \leq 7 \text{ kJ/mol}$  and  $0 \leq \delta \leq 8.5$  . To sum up, CrFeCoNiNb clad layer satisfies the criterion standard solid solution is formed.

Table. 2 Calculated results of  $\Delta S_{\text{conf}}$ ,  $\Delta H_{\text{mix}}$  and  $\delta$  of CrFeCoNiNb cladded layer

coating	$\Delta S_{\text{conf}}$	$\Delta H_{\text{mix}}$ (kJ/mol)	$\delta$
CrFeCoNiNb	13.37	-14.88	0.23

The laser process parameters are comprehensively acting on the cladded layer in the form of energy density. According to formula (1-4), five sets of energy density values are calculated. From Table 3, it can be seen that  $K$  satisfies the new criterion[19] proposed for the first time:  $0.04 \leq K \leq 0.14 \text{kJ} \cdot \text{m}^{-2}$ .

Table. 3 The specific laser power corresponding to different energy density

Sample	Power/W	Energy density(kJ/mm <sup>2</sup> )
1	800	0.0667
2	1 000	0.0833
3	1 200	0.1000
4	1 400	0.1167
5	1 600	0.1333

According to the Gibbs free energy equation (1-7), the  $\Delta G \sim T$  diagram is shown in Fig.2. It can be seen from Fig.2 that the reaction can proceed spontaneously in a positive direction. The entropy increases as the temperature increases, which leads to a decrease in the Gibbs free energy and thus a more stable system.

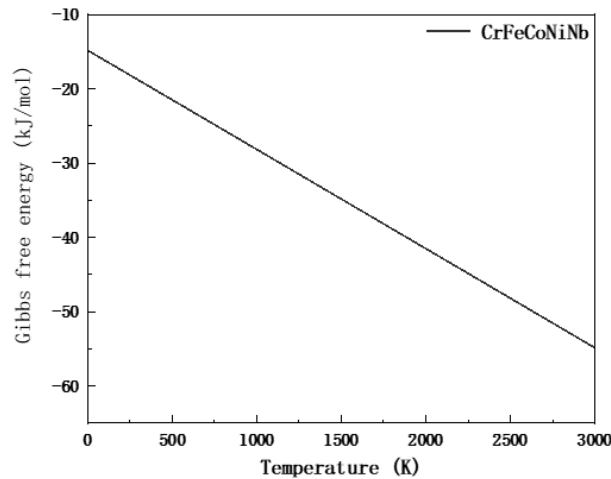


Fig.2. The Gibbs free energy of CrFeCoNiNb cladded layer varies with temperature.

### 3. Experimental

Five sets of tests are carried out on the basis of satisfying the thermodynamic criterion, and the symbols are shown in Table 3. The laser power is selected as a

variable to change the laser energy density. The scanning speed and spot diameter are fixed values, which are 3mm/s and 4mm respectively. Geometric characteristic parameters of the selected cladded layer include pool depth ( $D$ ), width ( $W$ ) and height ( $H$ ) of the single cladded layer. As shown in Fig. 3, the part where the substrate and the cladded powder are mixed and melted is called the molten pool, and the part that is not affected by heat is the substrate. The part of the substrate that is not melted by heat is called the transition zone and the heat-affected zone. The existence of the transition zone provides an effective buffer to prevent the interface cracking between the hard cladded layer and the soft substrate.

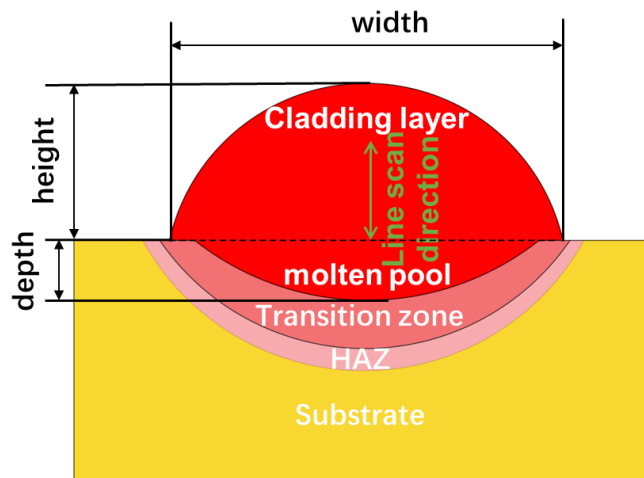


Fig.3. Cross section diagram of a single cladded layer.

The laser cladded layer of single-channel CrFeCoNiNb HEA on the 42CrMo substrate is carried out by preset powder method. The substrate is obtained by wire cutting with a size of 75mm×15mm×10mm, and its chemical composition was shown in Table 4. The surface of the substrate is sanded with 150# and 400# sandpaper successively, then it is cleaned with anhydrous ethanol and dried. The cladded layer is made of 200-400 mesh high-purity powder. According to the scanning electron microscope analysis of Fig. 4, the obtained powder is spherical, and the proportioning parameters are shown in Table 5. After ball milling for 2 hours, the prepared powder is kept at a constant temperature of 99 °C for drying for 2 hours. The length of the pre-spread powder is set as 65 mm and the thickness is controlled as 1 mm. After that, laser cladded is carried out on the smooth surface of the substrate. The applied cladded equipment is made up of German ROFIN FL020 fiber laser and KUKA-KR30 mechanical arm. In the whole cladded process, argon gas with purity of 99.99% is used to protect the molten pool from oxidation.

Table. 4 chemical composition of substrate

Element	C	Si	Mn	Cr	Ni
wt. %	0.38 ~	0.17 ~	0.5 ~ 0.8	0.90 ~	≤0.030
	0.45	0.37		1.20	
Element	P	S	Cu	Mo	Fe
wt. %	≤0.035	≤0.035	≤0.030	0.15 ~	Bal
				1.25	

Table. 5 Powder parameters

Element	Fe	Co	Ni	Cr	Nb
Purity	99.5%	99.4%	99.5%	99.5%	99.5%
wt. %	17.5%	18.5%	18.5%	16.3%	29.2%
Relative atomic mass	55.84	58.93	58.69	52.00	92.91
melting point	1811K	1768K	1728K	2180K	2750K
crystal structure	BCC	Hexagonal	FCC	BCC	BCC

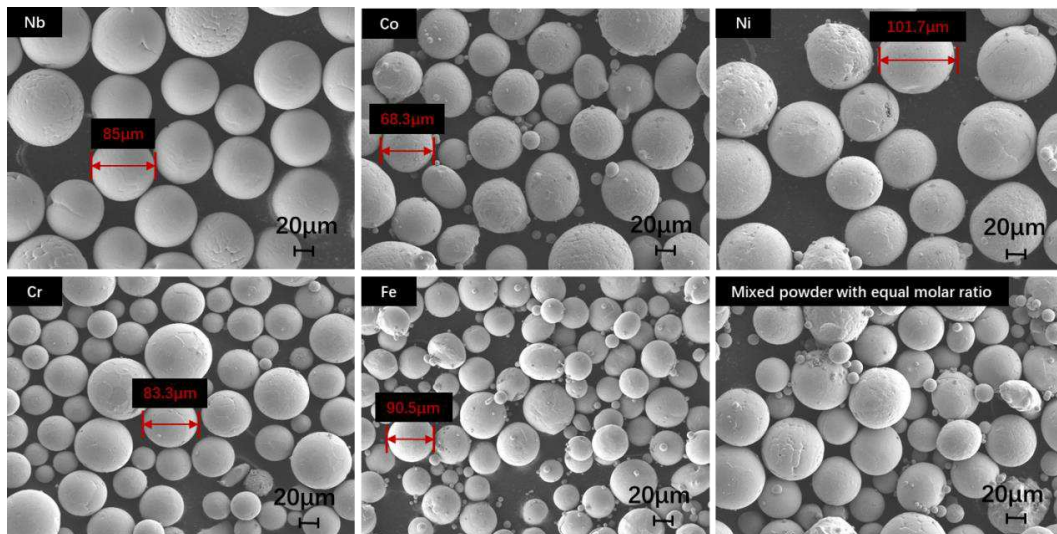


Fig.4. Morphological characteristics of CrFeCoNiNb powder.

The wear coefficient of the specimen is determined by the UMT-3 friction and wear tester. A  $\text{Si}_3\text{N}_4$  ball with a diameter of 9.5mm is applied as the friction pair. The setting parameters in the friction and wear test are as followings: the frequency is 2Hz, and the load is set as 10N, and the scratch length is 6mm, and the test time is set as 30min. Before the friction and wear test, the cladded layer is ground to a flat surface by a grinder. The electrochemical workstation CHI660E is used to test the

electrochemical property of the cladded layer, and 3.5wt.% NaCl solution is used as the corrosive medium. The sample is used as the working electrode, and the saturated calomel is used as the reference electrode (SCE) and Pt electrode is applied as the auxiliary electrode. The standard three-electrode system is used to test the action potential polarization. All the potentials described in this paper are measured by SCE. The scanning range of the polarization test potential is -2V ~ +1V, and the scanning rate is 1mV/s. Before the test, the sample is immersed in 3.5wt.% NaCl solution for 30min, so that the corrosion solution could invade the measured surface uniformly and stably, so as to ensure the accuracy of the results. Before these tests, the open circuit potential (OCP) is recorded for 30min to obtain a stable potential. An impedance test is performed at the corresponding open circuit potential, which is followed by a polarization test. All electrochemical tests are repeated at least 3 times to confirm the repeatability of the data and to provide representative data.

## **4. Results and discussion**

### **4.1 Phase composition**

The XRD patterns of CrFeCoNiNb cladded layers at different energy densities are shown in Fig. 5, and the main diffraction peaks are all BCC solid solution. There are significant differences in atomic size, electronegativity, and valence electron concentration among different atoms in the design elements. The lattice distortion caused by these differences will play a leading role in the phase composition of the cladded layer. In addition, the change of laser energy density does not change the main phase composition of the cladded layer, but causes local phase transformation. The change of phase change structure and inhomogeneity will affect the friction resistance and corrosion resistance of the cladded layer. It is found that BCC solid solution[20]is beneficial to improve the hardness of cladded layer. Moreover, high temperature is an important factor affecting the thermal stability of the solid solution. Intermetallic compounds will form when there is no thermal stability of the mixture. The lattice distortion is caused by the changing of input energy, while the main phase composition basically remains unchanged. It could be found in Fig. 5 that there are some tiny raised peaks between the main peaks, which are mainly composed of intermetallic compounds such as Cr<sub>2</sub>Nb. On the one hand, the existence of intermetallic compounds will weaken the structural stability of the cladded layer. On the other hand, the Nb-containing hard particles play a role of dispersion

strengthening for the fixing of dislocation[21].

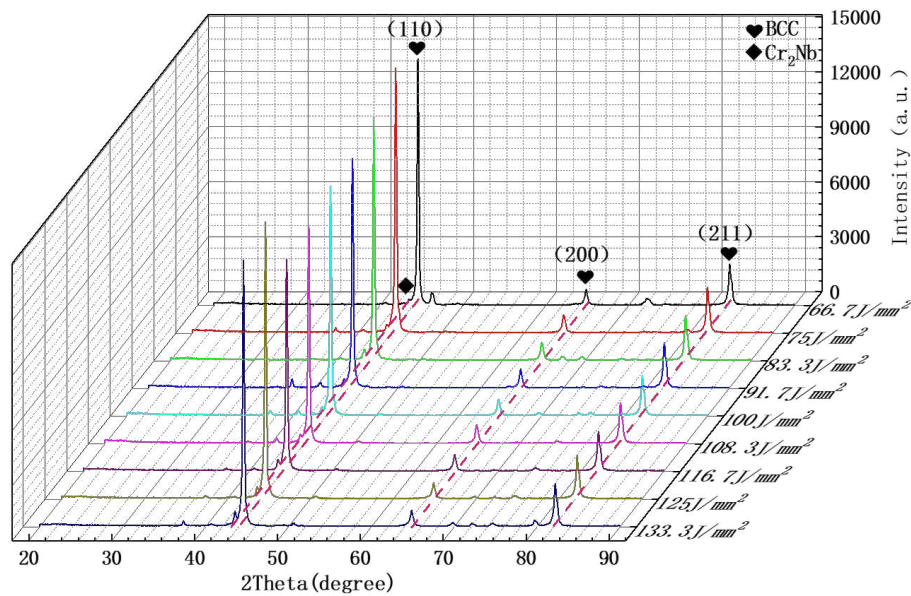


Fig.5. XRD patterns of CrFeCoNiNb clad layer at different energy density.

#### 4.2 Microstructure morphology

The macroscopic morphology and the variation trend of the width of the clad layer prepared under the energy density of  $66.7\text{J/mm}^2$  to  $133.3\text{J/mm}^2$  respectively are shown in Fig. 6. It could be observed that the heat input per unit area increases with the increase of laser energy density, and the powder melting area becomes larger, which leads to the increasing of the width of the clad layer.

The cross-section morphology of the clad layer is shown in Fig. 6c. It could be found that the cross-section morphology of the CrFeCoNiNb clad layer presents a "crescent shape". The crescent shape of clad layer could be due to the Gaussian distribution of the energy density of the laser beam, with high energy at the center and low energy at the edge. It is observed that there is a clear arc between the molten pool and the heat affected zone of the substrate, indicating that metallurgical bonding is formed between the clad layer and the substrate. When the laser energy density is  $66.7\text{J/mm}^2$ , there is little melting on the substrate surface, even if there is metallurgical bonding between the clad layer and the substrate. And also, the dilution rate is low, so the clad layer is easy to flake off. When the laser energy density reaches over  $83.3\text{J/mm}^2$ , a good metallurgical bonding is formed between the clad layer and the substrate, which is better than that of the alloy with mechanical bonding. The numerical relation diagram of the molten pool depth changing with the energy density is shown in Fig. 6d. The input of Gaussian heat source increases with

the increase of energy density. Since the input of Gaussian heat source increases with the increase of energy density, the molten pool depth is proportional to the energy density and more powder can be melted in the vertical direction.

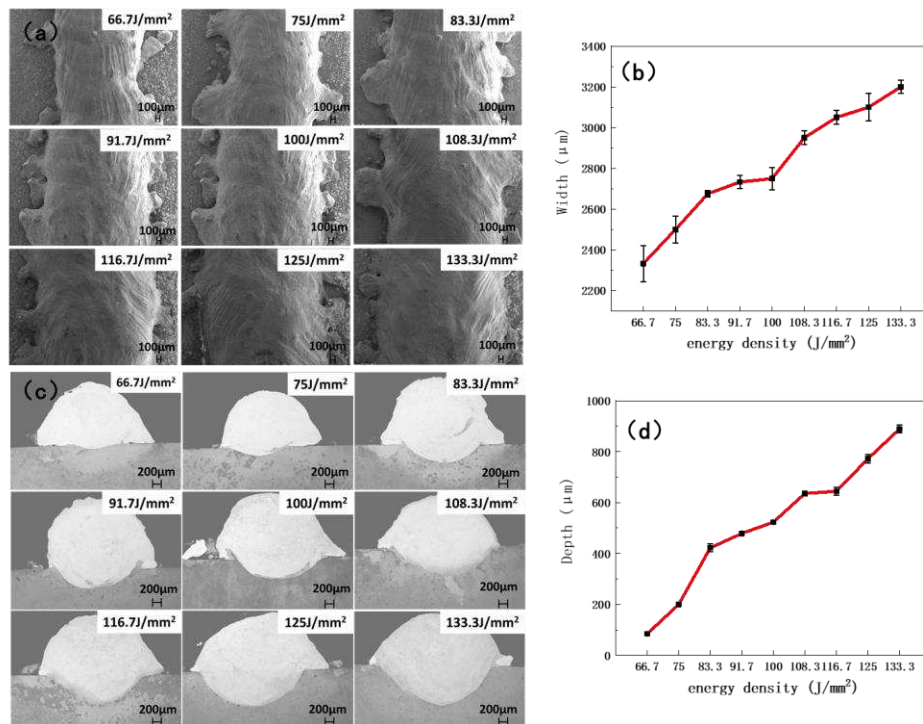


Fig.6. Macro morphology of cladded layer at different energy densities:

- (a)Cladded layer width, (b)Relationship between cladded width and energy density, (c)Depth of molten pool, (d)Relationship between depth of molten pool and energy density.

The molten pool is characterized by directional solidification, and the crystals in the direction of the fastest heat dissipation will grow preferentially, which makes the growth of dendrites perpendicular to the bottom of the molten pool far greater than that parallel to the bottom of the molten pool. The temperature gradient, solidification rate and their ratio determine the crystal morphology in the rapid solidification process of laser cladded. The crystalline morphology develops from plane grains to dendritic, cellular and equiaxed grains from the metallurgical bonding line to the direction of the cladded layer, which can be explained by the one-dimensional thermal conductivity model.

As shown in Fig. 7, the surface morphology of the cladded layer has a typical dendritic structure. During the initial solidification of the molten pool, the temperature of the matrix is low, resulting in a large temperature gradient  $G$  at the bottom of the molten pool. While the cooling rate  $R$  is very small, so that the  $G/R$  tends to infinity. Thus, the non-uniform grain nucleation, planar growth, the formation of planar crystal.

The middle part of the cladded layer is mainly columnar dendrite. At this point, the cladded layer radiates heat towards the substrate, and the  $R$  gradually increases, while the  $G/R$  value gradually decreases. Therefore, the planar crystal nucleation is difficult, and the thick columnar crystals are generated. With the increase of the thickness of the cladded layer, the heat dissipation rate decreases, so that  $G$  decreases,  $R$  increases, and  $G/R$  further decreases. As a result, the nucleation rate increases and finer cellular grains and equiaxed grains are formed at the top of the cladded layer. The existence of cellular crystals is due to the fact that cellular crystals are intermediate products of the transformation from columnar dendrites to equiaxed crystals.

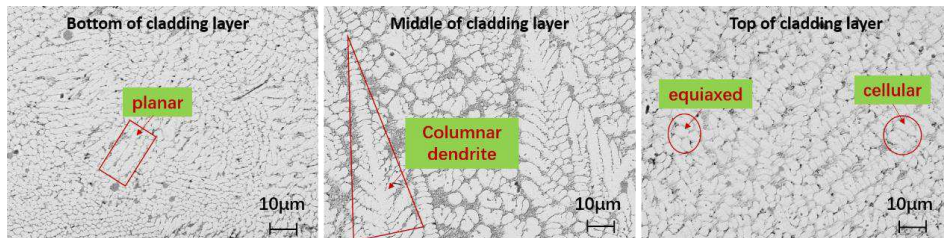


Fig.7. Grain morphology of cladded layer.

The grains in the top area of the cladded layer corresponding to different energy densities are shown in the Fig.8. It could be observed that the grain size varies with different energy densities. In an appropriate range, grain density increases with the increase of energy density, and the grain size refinement can be attributed to the inhibition of grain boundary migration[22] by dispersion particles. However, the high energy density ( $125\text{J}/\text{mm}^2$ - $133.3\text{J}/\text{mm}^2$ ) will increase the residence time at high temperature and coarsen the grain.

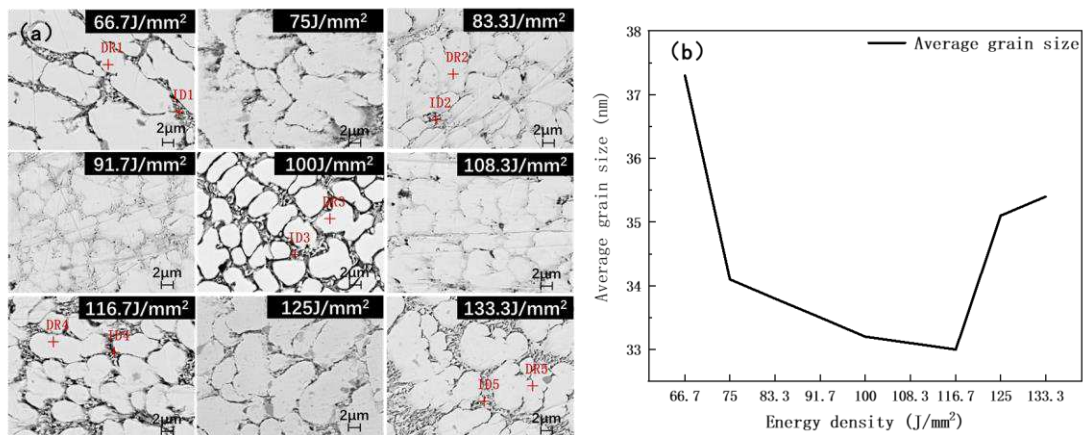


Fig.8. Grain size at top of cladded layer at different energy density.

DR and ID represented dendrite and interdendritic structure respectively. The

chemical compositions of the two parts were studied by EDS, according to carbides are distributed along grain boundaries and the content of Nb element in the DR is high, as listed in Table 6. It suggests that Nb element has a strong solute dragging effect[23], which can effectively prevent the migration of the interface. The non-equilibrium chemical boundary[24] formed by it plays a good role as a barrier.

Table. 6 Elemental content distribution (at %).

position	element							
	C	O	Cr	Fe	Co	Ni	Nb	Mo
DR1	15.44	0.46	15.06	15.33	18.45	14.47	20.4	0.39
ID1	29.84	7.5	11.72	13.81	13.08	14.36	9.43	0.26
DR2	14.2	0.26	15.91	20.78	14.76	13.11	20.45	0.54
ID2	26.32	8.52	9.83	15.26	12.46	14.44	12.68	0.49
DR3	12.86	0	14.94	24.61	14.97	12.61	19.55	0.46
ID3	33.39	5.39	11.09	18.14	9.65	10.04	11.82	0.48
DR4	13.03	0	14.55	29.18	13.51	11.09	18.32	0.32
ID4	26.25	11.56	5.78	20.59	10.82	10.41	14.08	0.5
DR5	17.9	0	18.97	15.27	16.41	13.56	17.45	0.44
ID5	18.11	0	21.22	16.44	15.23	19.96	8.88	0.15

In order to analyze the elemental partitioning behavior in the energy density range from  $66.7\text{J/mm}^2$  to  $133.3\text{J/mm}^2$ , the EDS line scan performs on the green line on Fig. 3, and the distributions of different alloying elements are shown in Fig9. It is observed that Fe, Co, Ni and Cr are fully and uniformly dissolved, and their diffraction peaks have roughly the same vibration wave direction. The highest wave peak of the diffraction peak of Nb element corresponds to the trough of these four elements, which corresponds to the content distribution of DR and ID in Table. 6. The highest wave peak of the diffraction peak of Nb element corresponds to the trough of these four elements, which corresponds to the elements distribution of DR and ID in Table 6. Moreover, with the increase of energy density, the content of Fe has an upward trend. It is inferred that the diffusion behavior of Fe element occurs with the increase of temperature. Through diffusion, the solute components in BCC solid solution exceed the solution limit and form new phases continuously.

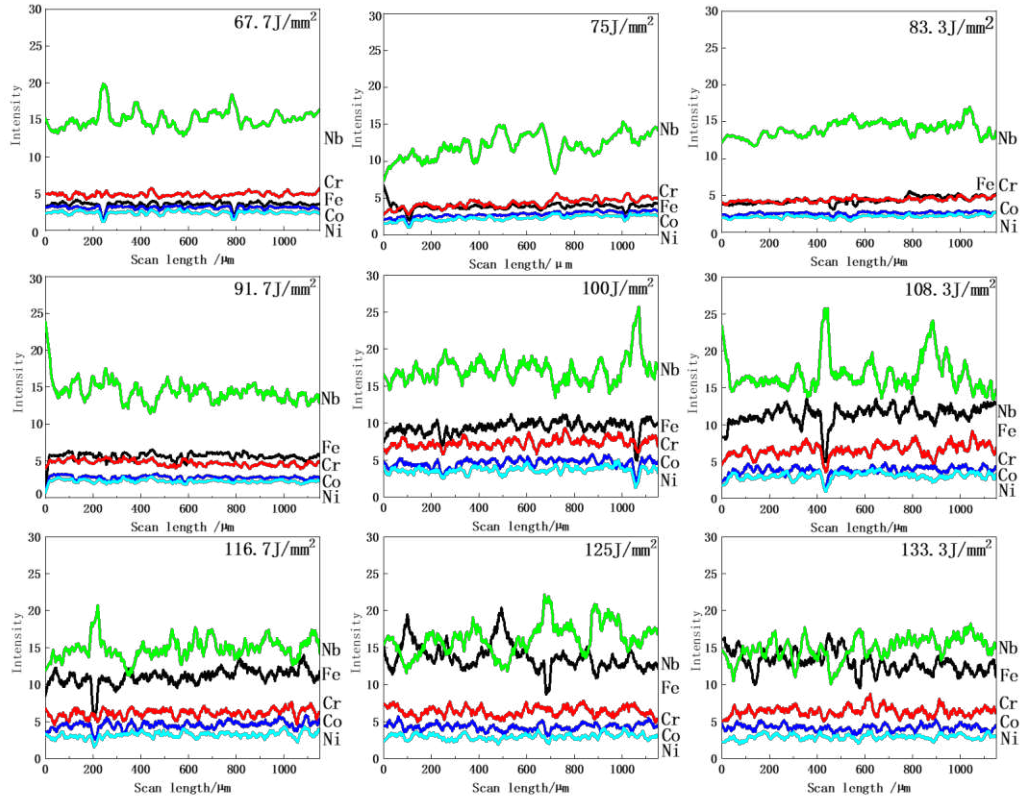


Fig.9. EDS line scan results of cladded layer at different energy density.

### 4.3 Microhardness

In order to investigate the influence of energy density on the mechanical properties of CrFeCoNiNb cladded layer, the surface microhardness of the cladded layer was measured as shown in Fig. 10. The results show that the microhardness of the cladded layer at different energy density, 625~729 HV<sub>0.98</sub>, is significantly higher than that of the 42CrMo substrate, 200 HV<sub>0.98</sub>. It means that HEAs coating with high microhardness, which is attributed to the solution strengthening caused by the high size mismatch between Nb with Co, Cr, Fe, and Ni, as well as the formation of BCC strengthening phase, can effectively improve the comprehensive mechanical property of the substrate. The five elements in the cladded layer belong to transition metal elements, and their electronegativity is about 1.6~1.9. The difference of electronegativity is small, and the dominant trend is to generate solid solution. The solid solution strengthening effect produced by BCC solid solution has a dominant influence on the hardness of cladded layer. Grain refinement produces Hall-Petch effect, which has relatively little effect on the hardness of cladded layer. With the increase of energy density from 66.7J/mm<sup>2</sup> to 116.7J/mm<sup>2</sup>, the diffraction peak area of BCC phase decreases. The effect of solid solution strengthening of BCC hard phase

on the hardness of cladded layer covers up the effect of grain refinement, and the hardness of cladded layer decreases continuously. When the energy density increases from 116.7J/mm<sup>2</sup> to 133.3J/mm<sup>2</sup>, the diffraction peak area of BCC hard phase increases. The effect of solution strengthening on the hardness of the cladded layer overcovers the effect of grain coarsening, and the hardness of the cladded layer has a tendency to increase. refining strengthening effect.

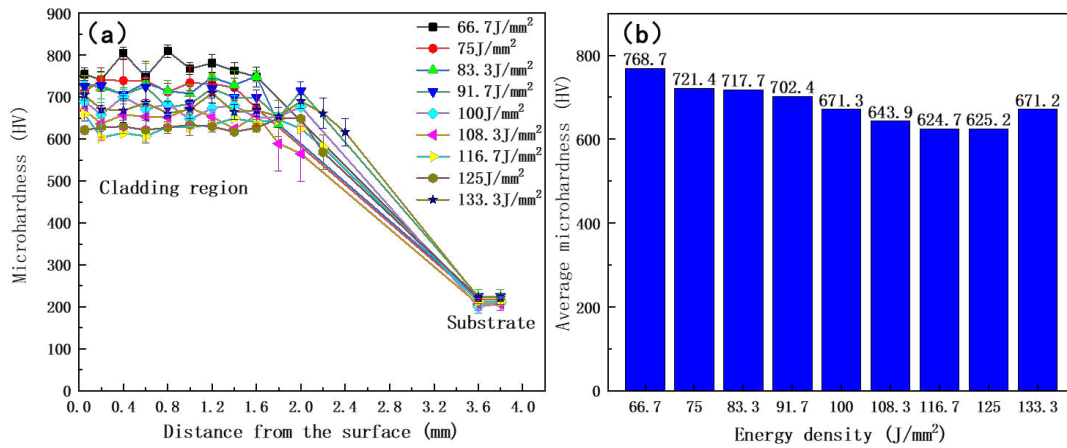


Fig.10. Microhardness of cladded layer varies with energy density:  
(a)Microhardness distribution; (b)Mean value of microhardness.

#### 4.4 Antifriction and wear resistance

As can be seen from Fig. 11(a), the friction coefficient is very small due to the smooth surface of the substrate, when Si<sub>3</sub>N<sub>4</sub> spheres are in contact with the substrate. Then, with the repeated sliding movement, the worn surface cracks under the shear stress, resulting in the formation of flakes and wear debris on the tribolayer, friction coefficient increases linearly. After that, the friction coefficient tends to be stable because the flakes generated between the friction pair and the friction layer plays the role of lubrication[25]. In addition, the flat and smooth tribolayer is also beneficial to stabilize the friction coefficient.

The quality of antifriction can be characterized by the level of friction coefficient[26]. When the laser energy density is 116.7J/mm<sup>2</sup>, the friction coefficient of the cladded layer is the smallest as shown in Fig. 11(b). Combined with the peak area of XRD, the diffraction peak area of impurity phase in the cladded layer prepared at 116.7J/mm<sup>2</sup> is significantly reduced, and the cladded layer has a more uniform element distribution. In the process of sliding wear, the corresponding antifriction property is better, which is conducive to reducing the friction loss of the cladded layer and improving the use efficiency of friction pair.

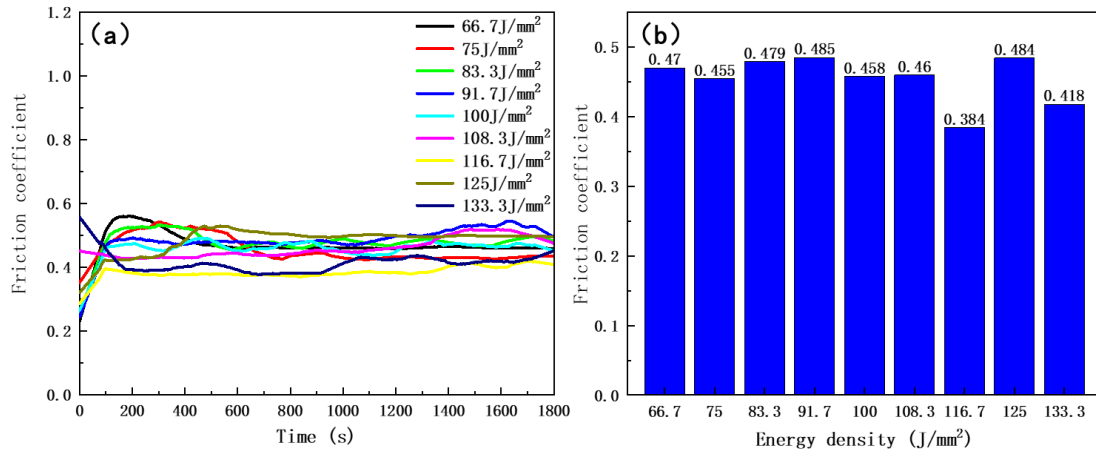


Fig. 11. Friction coefficient in cladded region varies with energy density:

(a)Friction coefficient curve, (b)Mean value of friction coefficient.

The wear morphology of cladded layer under different energy densities is illustrated in Fig. 12(a). During the sliding wear test, adhesion is easy to occur between the friction pair and the worn surface, and the spalling sheet produced is the main feature of adhesion wear. As the third body, the wear debris of the friction interface plows the friction surface, which is the main feature of abrasive wear. There are furrows, flakes, spalling crater and wear debris on the surface of the cladded layer, indicating that the wear mechanism is adhesive wear and abrasive wear. When the energy density ranges from 66.7J/mm<sup>2</sup> to 108J/mm<sup>2</sup>, the furrow on the worn surface is not obvious, and the combination between the flakes and the worn surface is firm and smooth. Apparently, the cladded layer is mainly adhesive wear, and the friction coefficient is large. When the laser energy density is 116.7J/mm<sup>2</sup>, the tribolayer is relatively smooth and shows wide and deep furrows, which is largely related to the lower hardness value. Notably, the wear surface is relatively smooth, mainly consisting of fine furrows, a small amount of wear debris, a small amount of spalling crater and flakes, indicating the occurrence of abrasive wear, and the friction coefficient is minimal. When the energy density is in the range of 125J/mm<sup>2</sup> to 133.3J/mm<sup>2</sup>, new flakes are produced between the furrows, and the surface roughness is higher. This makes sense, since the combination with the worn surface is not strong, which promotes the surface damage[27]and leads to a large friction coefficient.

Wear resistance refers to the resistance of the material itself to wear. According to the Achard relation[28], the hardness distribution is proportional to the wear resistance. In addition, a large number of literatures[29] also indicate that the wear

resistance of the cladded layer with high hardness is relatively better. According to the Achard equation, the wear rate is inversely proportional to hardness:

$$Q = \frac{K \cdot D \cdot F}{H} \quad [32]$$

Where,  $Q$  is the wear rate,  $K$  is the friction coefficient,  $D$  is the sliding distance,  $F$  is the applied load, and  $H$  is the hardness of the worn surface.

According to Fig. 11(b), the wear rate increases first and then decreases with the increase of energy density, which is almost proportional to the hardness distribution. However, the cladded layer prepared at the laser energy density of  $116.7 \text{ J/mm}^2$  has the best antifriction effect, so its wear resistance is better, and the wear rate tends to decrease.

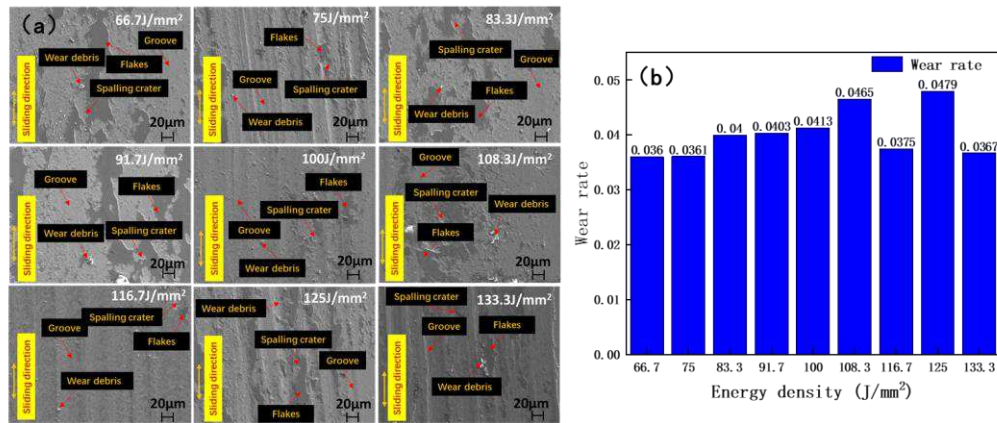


Fig.12. The wear morphologies of cladded layer at different energy density:

(a) wear morphologies; (b) wear rate.

#### 4.5 Corrosion resistance

In order to study the influence of energy density on corrosion resistance of CrFeCoNiNb cladded layer on 42CrMo substrate, potentiodynamic polarization curves were measured in 3.5wt.% NaCl solution. As shown in Fig. 13(a), it is obvious that the corrosion resistance of the cladded layer is significantly improved compared with the substrate. Moreover, Obviously, due to the mixing of passivation accelerator (Cr)[33], solution-blocker (Nb)[33] and base elements (Fe, Co, Ni)[33] produces a very corrosion-resistant BCC single-phase structure, resulting the potential polarization curve shows a wide passivation region, which indicates that the passivation occurs spontaneously.

It is generally believed that the corrosion resistance of the cladded layer with high self-corrosion potential is relatively better, which is mainly based on the thermodynamic possibility of corrosion, while ignoring the corrosion dynamics.

Therefore, the corrosion resistance of a material can not be accurately judged by the self-corrosion potential alone. On the contrary, self-corrosion current is related to corrosion dissolution, and the value of self-corrosion current or corrosion current density can be used as an important parameter to evaluate the corrosion resistance of a material. According to Fig. 13(b), the self-corrosion current of cladded layer decreases first and then increases with the increase of laser energy density. Among them, the variation trend of the corrosion current is consistent with that of the corrosion current density in the polarization curve. Here, it is worth mentioning that grain refinement can improve the compactness of the passivation film on the surface of the cladded layer, and the passivation film with high density can improve the corrosion resistance of the cladded layer. When the laser energy density increases from  $66.7\text{J}/\text{mm}^2$  to  $100\text{J}/\text{mm}^2$ , the passivation film becomes more compact due to the continuous refinement of the grain size, and the  $I_{\text{corr}}$  tends to decrease. However, when the laser energy density is greater than  $116.7\text{J}/\text{mm}^2$ , the grains appear coarsening due to the high temperature, resulting in a decrease in the passivation film density and a decrease in the corrosion resistance of the cladded layer.

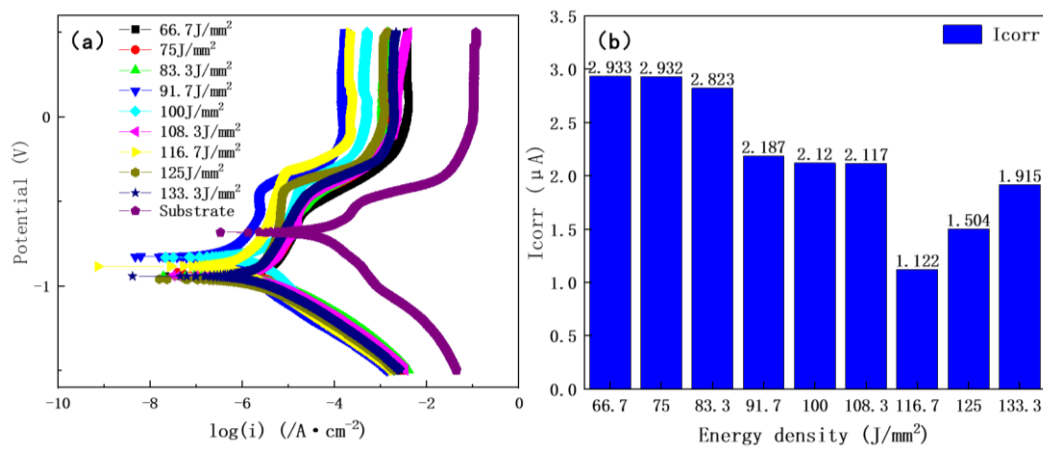


Fig.13. Corrosion behavior of CrFeCoNiNb cladded layer vary with energy density: (a)Polarization behavior in 3.5wt.%NaCl solution, (b)The trend of self-corrosion current.

Next, we examined the surface morphologies of the cladded layer at different energy density as shown in Fig. 14. Since the high solubility of NaCl and the small radius of  $\text{Cl}^-$ , these  $\text{Cl}^-$  have the most prominent destructive effect on passivation film. For the same cladded layer prepared under different laser energy densities, the stability of the passivation film is also one of the reasons that affect the corrosion resistance. Therefore, the stability of the passivation film is also one of the factors affecting its corrosion resistance. In addition, the ability to form a continuous

passivating film without component defects on the passivated alloy surface is one of the key factors in determining the pitting resistance, since pitting occurs preferentially on the passivated non-uniform surface.

Inhomogeneity in the microstructure, such as segregation of impurity phases or elements, is detrimental to the continuity of the passivated film because oxides formed at or around these locations usually have no protective effect. It is found that when the energy density is  $116.7\text{J}/\text{mm}^2$ , the diffraction peak area of the impurity phase is less. And when the energy density is too high or too low, the area of the diffraction peak of the impurity phase increases relatively. Although the energy density changes, only some pitting pits and intergranular corrosion phenomena can be found locally, because CrFeCoNiNb cladded layer is very corrosion resistant. Except the formation of some pitting pits at the segregation of Nb and Cr elements, pitting pits are also formed at the intergranular corrosion. The intergranular corrosion destroys the bond between grains, which leads to the loosening of grains and the formation of pitting pits. Notably, with the increase of laser energy density, the grain is refined and the intergranular corrosion zone becomes narrower and smaller. And it is not easy to form pitting pits since its loosening effect on grains is small, and the intergranular corrosion zone becomes narrow and small, which has less loosening effect on the grain and is not easy to form pitting pits. However, when the laser energy density exceeds  $116.7\text{J}/\text{mm}^2$ , the excessively high energy density leads to grain coarsening and the intergranular corrosion region becoming wider. At this point, the loosening effect between grains is strengthened and pitting pits are easily formed.

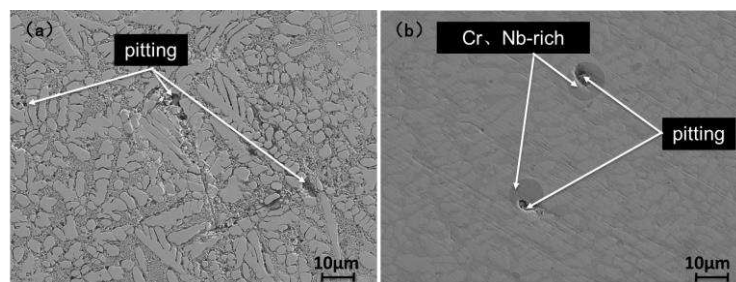


Fig.14. Corrosion morphology of CrFeCoNiNb cladded layer at different energy density:

(a) Pitting at intergranular corrosion, (b) Pitting at segregation.

## 5 Conclusion

In a large part, the technological parameters of laser cladded determine the performance of the cladded layer. Different laser energy densities will lead to different uniformity of microstructure and different grain refinement degree, which directly affect

the mechanical properties and corrosion properties of the cladded layer. The main findings can be summarized as follows:

(1) Macroscopically, it is found that the depth and width of molten pool increase with the increase of energy density, and the growth rate of depth is greater than that of width. The cladded layer prepared by low energy density is not firmly bonded with the substrate and is easy to flake off, while too high energy density will lead to the waste of resources. From the microstructure point of view, the CrFeCoNiNb cladded layer is mainly composed of BCC solid solution. The bottom of the cladded layer is planar crystals, the middle is mainly columnar dendrites, and the top is equiaxed crystals and cellular crystals.

(2) As the energy density increases, the BCC solid solution content decreases first and then increases, and the grains of the cladded layer are first refined and then coarsened. The grain refinement strengthening effect produced by grain refinement and the solid solution strengthening effect produced by the BCC phase work together on the cladded layer, but the solid solution strengthening effect plays a leading role in the change trend of the cladded layer's microhardness. In addition, the wear resistance of the cladded layer is also proportional to the hardness, but when the energy density is  $116.7\text{J}/\text{mm}^2$ , the cladded layer has the best antifriction effect, resulting in a decrease in the wear rate.

(3) For the same CrFeCoNiNb cladded layer with different laser energy densities, the corrosion resistance is mainly related to the compactness and stability of the passivation film. The uniformity of phase distribution directly affects the stability of the passivated film, and the density of grain is closely related to the density of the passivated film, which are the main factors affecting the corrosion resistance of the cladded layer.

### **Acknowledgements**

**Funding:** This work was financially supported by the Key Research and Development Program of Shandong Province (2019GNC106102), and the Natural Science Foundation of Shandong Province (R2019MEE059, ZR2018PEE011, ZR2019PEE041).

**Conflicts of interest:** We declare that we do not have any commercial or associative interest that represents a conflict of interest in connection with the work submitted.

**Availability of data and material:** Not applicable

**Code availability:** Not applicable

**Ethics approval:** Not applicable

**Consent to participate:** Not applicable

**Consent for publication:** Not applicable

## References

- [1] Yeh J W (2013) Alloy design strategies and future trends in high-entropy alloys. *Miner Met Mater Soc* 65(12):1759-1711.
- [2] Nene S S, Frank M, Liu K, Sinha S, Mishra R S (2020) Corrosion-resistant high entropy alloy with high strength and ductility. *Scripta Materialia* 166:168-172.
- [3] Ding, Q Q, Zhang Y, Chen X, Fu X, Chen D, Chen S (2019) Tuning element distribution, structure and properties by composition in high-entropy alloys. *Nature* 574(7777):223-227.
- [4] Dong Y, Yao Z, Huang X, Du F, Zhang Z (2020) Microstructure and mechanical properties of  $\text{AlCo}_x\text{CrFeNi}_{3-x}$  eutectic high-entropy alloy system. *J Alloys and Compounds* 823:153886.
- [5] Malyt T, Prashanth K G, Janda A, Kim J T, Spieckermann F, Eckert J (2019) Mechanism of high-pressure torsion induced shear banding and lamellae thickness saturation in Co-Cr-Fe-Ni-Nb high entropy composites. *Journal of Materials Research* 34(15):2672-2682.
- [6] Xie T, Xiong Z, Xu Z, Liu Z, Cheng X (2021) Another eutectic point of Co–Cr–Fe–Ni–M (Hf, Ta, Nb) high-entropy system determined using a simple mixture method correlated with mixing enthalpy. *Materials Science and Engineering A* 802:140634.
- [7] Chaturvedi M C, Chung D W (1981) Yielding behavior of a  $\gamma$ -precipitation strengthened Co Ni Cr Nb Fe alloy. *Metallurgical Transactions A* 12(1):77-81.
- [8] Tsau C H, Yeh C Y, Tsai M C (2019) The effect of Nb-content on the microstructures and corrosion properties of  $\text{CrFeCoNiNb}_x$  high-entropy alloys. *Materials* 12(22):3716.
- [9] Zhang M, Zhang L, Liaw P K, Li G, Liu R (2018) Effect of Nb content on thermal stability, mechanical and corrosion behaviors of hypoeutectic  $\text{CoCrFeNiNb}_x$  high-entropy alloys. *J Materials Research* 33(19):3276-3286.
- [10] Wang W, Wu Q, Lu X, Xiao Y, Li J, Zhang Y (2019) Microstructure and corrosion behavior of  $(\text{CoCrFeNi})_{95}\text{Nb}_5$  high-entropy alloy coating fabricated by plasma spraying. *Materials* 12(5):1-12.
- [11] Yang X, Deng W, Huang X, Tian L (2014) Research on preparation methods of high-entropy alloy. *Hot Working Technology*, 2014:129-138.
- [12] Liu Y, Ding Y, Yang L, Sun R, Yang X (2021) Research and progress of laser cladded on engineering alloys: A review. *J Manufacturing Processes* 66(1):341-363.
- [13] Lt A, Af A, Lc B (2020) CoCr alloy processed by selective laser melting (SLM): effect of laser energy density on microstructure surface morphology and hardness. *J Manufacturing Processes* 52:106-119.
- [14] Biswas K, Yeh J W, Bhattacharjee P P, Hosson J (2020) high entropy alloys: key issues under passionate debate. *Scripta Materialia* 188:54-58.

- [15] Cong N, Yan S, Jia L, Huang G (2018) Characterization of  $\text{Al}_{0.5}\text{FeCu}_{0.7}\text{NiCoCr}$  high-entropy alloy coating on aluminum alloy by laser cladded. *Optics & Laser Technology*, 105:257-263.
- [16] Yeh J W, Chen S K, Lin S J, Gan J Y, Chin T S, Shun T T (2004) Nanostructured high-entropy alloys with multiple principal elements: novel alloy design concepts and outcomes. *Advanced Engineering Materials* 6(5):299-303.
- [17] Zhang Y, Zhou Y J, Lin J P, Chen G L, Liaw P K (2008) Solid-solution phase formation rules for multi-component alloys. *Advanced Engineering Materials* 10(6):534-538.
- [18] Cd A, Sgr B B (2017) Hume-rothery for HEA classification and self-organizing map for phases and properties prediction-ScienceDirect. *J Alloys and Compounds* 724:353-364.
- [19] Juan Y F, Li J, Jiang Y Q, Jia W L, Lu Z J (2019) Modified criterions for phase prediction in the multi-component laser-clad coatings and investigations into microstructural evolution/wear resistance of  $\text{FeCrCoNiAlMo}_x$  laser-clad coatings. *Applied Surface Science* 465:700-714.
- [20] Shang C Y, Axinte E, Ge W J, Zhang Z T, Wang Y (2017) High-entropy alloy coatings with excellent mechanical, corrosion resistance and magnetic properties prepared by mechanical alloying and hot pressing sintering. *Tribology Materials Surfaces & Interfaces* 9:36-43.
- [21] Bate P (2001) The effect of deformation on grain growth in Zener pinned systems. *Acta Materialia* 49(8):1453-1461.
- [22] Liu P C, Wang Z X, Cong J H, Misra R Zhang Y Q (2020) The significance of Nb interface segregation in governing pearlitic refinement in high carbon steels. *Materials Letters* 279:2-3.
- [23] Suehiro M (1998) An analysis of the solute drag effect of Nb on recrystallization of ultra low carbon steel. *ISIJ International* 38(6):547-552.
- [24] Wang H H, Wang J, Tong, Z, Hodgson P D, Wan X L, Wu K M (2018) Characterization of Nb interface segregation during welding thermal cycle in microalloyed steel by atom probe tomography. *Metallurgical and Materials Transactions A* 49:2-5.
- [25] Khodabakhshi F, Simchi A, Kokabi A H (2016) Surface modifications of an aluminum-magnesium alloy through reactive stir friction processing with titanium oxide nanoparticles for enhanced sliding wear resistance. *Surface and Coatings Technology* 309:114-123.
- [26] Lv Tao, Huang Shuiquan, Hu Xiaodong (2018) Tribological and machining characteristics of a minimum quantity lubrication (MQL) technology using  $\text{GO/SiO}_2$  hybrid nanoparticle water-based lubricants as cutting fluids. *International Journal of Advanced Manufacturing Technology* 96 (5-8): 2931-2942.
- [27] Li Y, Su K, Bai P, Wu L (2020) Microstructure and property characterization of Ti/TiBCN reinforced Ti based composite coatings fabricated by laser cladded with different scanning speed. *Materials Characterization* 159:7-9.
- [28] Archard J F (1953) Contact and rubbing of flat surfaces. *J Applied Physics* 24(8):981-989.
- [29] Guo Y X, Shang X J, Liu QB (2018) Microstructure and properties of in-situ TiN reinforced

laser cladded  $\text{CoCr}_2\text{FeNiTi}_x$  high-entropy alloy composite coatings. *Surface and Coatings Technology* 344:353-358.

- [30] Ye X, Ma M, Cao Y, Liu W, Ye X, Yu G (2011) The property research on high-entropy alloy  $\text{Al}_x\text{FeCoNiCuCr}$  coating by laser cladded. *Physics Procedia* 12:303-312.
- [31] Chen H, Li H Q, Sun Y Z, Li M (2006) Microstructure and properties of coatings with rare earth formed by DC-plasma jet surface metallurgy. *Surface & Coatings Technology* 200(16-17):4741-4745.
- [32] Mazaheri Y, Jalilvand M M, Heidarpour A, Jahani A R (2019) Tribological behavior of  $\text{AZ}_{31}/\text{ZrO}_2$  surface nanocomposites developed by friction stir processing. *Tribology International* 143:106062.
- [33] Taylor C D, Lu P, Saal J, Frankel G S, Scully J R (2018) Integrated computational materials engineering of corrosion resistant alloys. *Materials Degradation*, 2(1):1-10.